Journal: NETWORK NEUROSCIENCE

RESEARCH

Brain signaling becomes less integrated and more segregated with age

Rostam M Razban¹, Botond B Antal^{2,5}, Ken A Dill^{1,4,6},

and Lilianne R Mujica-Parodi^{1,2,3,4,5}

1 Laufer Center for Physical and Quantitative Biology, Stony Brook University, Stony Brook, NY, USA

2 Dept. of Biomedical Engineering, Stony Brook University, Stony Brook, NY, USA

3 Program in Neuroscience, Stony Brook University, Stony Brook, NY, USA

4 Dept. of Physics and Astronomy, Stony Brook University, Stony Brook, NY, USA

5 Athinoula A. Martinos Center for Biomedical Imaging, Massachusetts General Hospital and Harvard Medical School, Boston, MA, USA

6 Dept. of Chemistry, Stony Brook University, Stony Brook, NY, USA

Keywords: [Aging, fMRI, dMRI, Statistical Physics]

ABSTRACT

- The integration-segregation framework is a popular first step to understand brain dynamics because it
- simplifies brain dynamics into two states based on global vs. local signaling patterns. However, there is
- 14 no consensus for how to best define what the two states look like. Here, we map integration and
- segregation to order and disorder states from the Ising model in physics to calculate state probabilities,
- $P_{\rm int}$ and $P_{\rm seg}$, from functional MRI data. We find that integration/segregation decreases/increases with age
- across three databases, and changes are consistent with weakened connection strength among regions
- rather than topological connectivity based on structural and diffusion MRI data.

AUTHOR SUMMARY

Authors: R.M. Razban, B.B. Antal, K.A. Dill, L.R. Mujica-Parodi

- The integration-segregation framework succinctly captures the tradeoff brains face between seamless
- function (more integration) in light of energetic constrains (more segregation). Despite its ubiquitous use
- in the field, there is no consensus on its definition with various graph theoretical properties being
- proposed. Here, we define the two states based on the underlying mechanism of neuronal coupling
- 23 strength to provide a physical foundation for the framework. We find that younger adults' brains are close
- to perfectly balancing between integration and segregation, while older adults' brains veer off towards
- 25 random signaling.

INTRODUCTION

- ²⁶ Aging is the number one risk factor for almost all neurodegenerative diseases (Kennedy et al., 2014). For
- every 5 years after the age of 65, the probability of acquiring Alzheimer's disease doubles
- ²⁸ (Bermejo-Pareja et al., 2008). An influential conceptual approach to begin making sense of brain
- ²⁹ dynamics frames it in terms of a balance between **integrated** and **segregated** network **states** (Deco,
- Tononi, Boly, & Kringelbach, 2015; Friston, 2009; Sporns, 2010, 2013; Tononi, Sporns, & Edelman,
- 1994; Wig, 2017). On one hand, the brain faces functional pressure to have as many regions directly
- connected for quick communication. On the other hand, the brain is constrained to minimize metabolic
- energy consumption because it consumes ten-times more of the body's energy than expected by mass
- ³⁴ (Raichle, 2006). Tuning the balance between extensive global signaling, referred to as integration, and
- limited local signaling, referred to as segregation, optimally compromises between functional and
- energetic constraints (Bullmore & Sporns, 2012; Cohen & D'Esposito, 2016; Manza et al., 2020; Wang
- et al., 2021). Although these constraints remain throughout life, aging disrupts their balance.
- Previous research found mixed aging results, depending on the metrics used to measure integration and
- segregation (Chan, Park, Savalia, Petersen, & Wig, 2014; Chen et al., 2021; Onoda & Yamaguchi, 2013;
- ⁴⁰ Zhang et al., 2021). Although most in the literature use the system segregation metric (Chan et al., 2014),
- 41 no consensus exists surrounding integration. In general, the problem facing the integration-segregation
- 42 framework is that there is no one way to define the two states. Many graph theoretical metrics could
- potentially be used (Rubinov & Sporns, 2010) and it is unclear why one should take precedence over the

Authors: R.M. Razban, B.B. Antal, K.A. Dill, L.R. Mujica-Parodi

- other, particularly when their aging outcomes are mutually inconsistent. There is a need to more
- fundamentally define integration and segregation to transform it from a proxy to a physical quantity.
- Here, we provide a physical foundation for the framework by applying the mean field **Ising model** to
- treat integration and segregation as physical 2-phase systems like magnets and liquids. After
- demonstrating that the Ising model can capture global brain dynamics as measured by functional MRI
- once the effective number of nodes is properly set, we proceed to calculate probabilities of being in the
- integrated or segregated states and find that younger and older brains are bounded by optimal and random
- signaling, respectively. We then explore diffusion and structural MRI data to ask if the age-related
- changes in signaling are due to changes in topological network connectivity.

APPLYING THE ISING MODEL TO FMRI

- ⁵³ We model human brain signaling patterns obtained from resting-state functional MRI (fMRI) data sets.
- As in previous work (Weistuch et al., 2021), we capture those patterns with the Ising model, a widely
- used theoretical method for expressing macroscale behaviors in terms of interactions among many
- underlying microscale agents (Dill & Bromberg, 2012). We first transform the continuous fMRI data into
- a representation as discrete Ising spins via binarization of the data (Figure 1). That is, we reduce the state
- of the region as either -1 or 1 based on whether fMRI signaling is decreasing or increasing, respectively.
- Second, we calculate the *synchrony* by summing over all spins in a given time interval and dividing by
- the total number of spins (Figure 1). Synchronies are collected over the entirety of the scan to obtain a
- distribution. Based on Ising model theory, the synchrony threshold delineating between integrated and
- segregated states is set such that $P_{\text{int}} = P_{\text{seg}} = 1/2$ at the Ising model's **critical point** (Methods). P_{seg} is
- the probability that the brain is in the segregated state and is defined as the relative number of time points
- for which the absolute value of synchrony is less than the synchrony threshold (Figure 1). P_{int} is defined
- as the relative number of time points for which the absolute value of synchrony is greater than the
- synchrony threshold and trivially relates to P_{seg} because $P_{\text{int}} + P_{\text{seg}} = 1$.

Authors: R.M. Razban, B.B. Antal, K.A. Dill, L.R. Mujica-Parodi

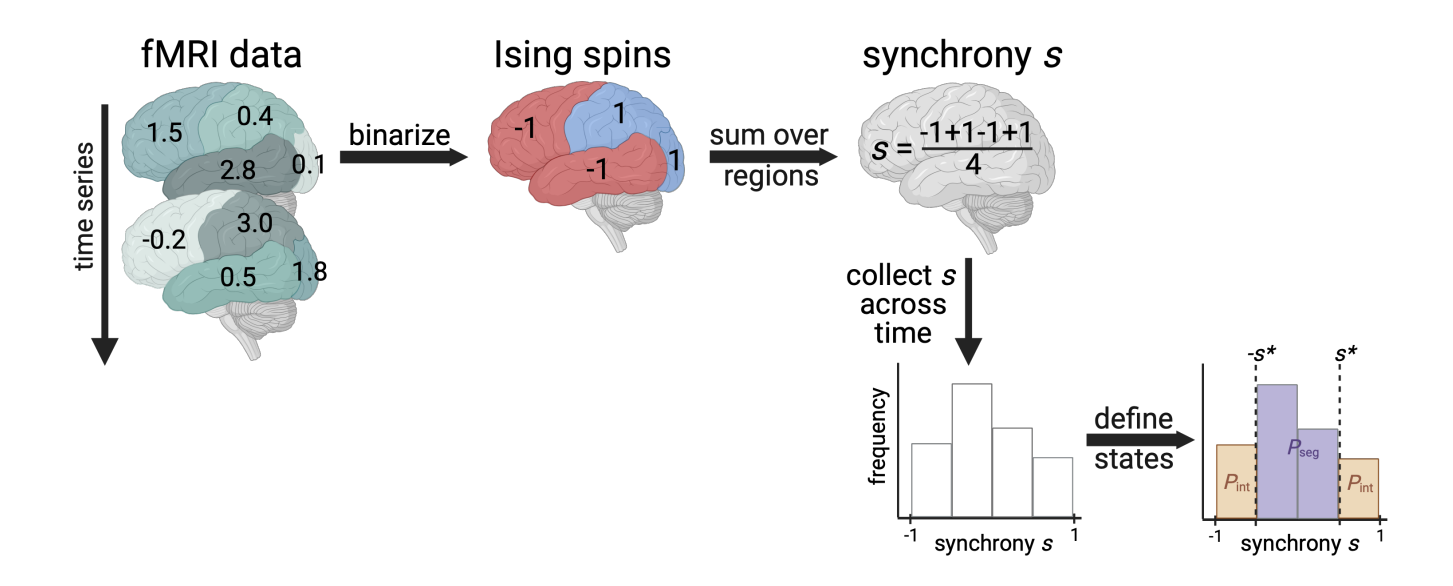


Figure 1. Calculating the probability that the brain exhibits integrated or segregated dynamics (P_{int} or P_{seg}). The schematic demonstrates the procedure for one individual's fictitious functional MRI scan with 4 brain regions and only two time points shown. First, we binarize data based on nearest neighbor scans in time. If the functional MRI (fMRI) signal increases, a value of 1 is assigned; decreases, -1. Then, we calculate the average spin state of the brain, called synchrony. Finally, we collect synchrony values across the entire time series to create a synchrony distribution. We appropriately set the synchrony threshold based on Ising model theory to delineate between integrated and segregated microstates. Additional details can be found in the Methods. Figure created with Biorender.com.

RESULTS

73 The number of functionally effective brain regions

Before proceeding to calculate $P_{\rm seg}$, we first check whether the model can capture the experimental synchrony distributions. A mean field Ising model only considering pairwise interactions has one quantity of interest. The strength of connection λ between any two regions corresponds to the degree to which signals between any two brain regions are correlated. However, we find that a naive fit of λ based on **maximum entropy** (Dill & Bromberg, 2012; Schneidman, Berry, Segev, & Bialek, 2006; Weistuch et al., 2021) fails to capture the synchrony distribution from fMRI data (Figure 2, orange). To improve upon a standard Ising model approach, here we introduce a hyper-parameter $N_{\rm eff}$. Brain atlas parcellations provide N brain regions, however, those N regions must be identically distributed across time for the Ising model to apply. We find that when setting N to a lower value $N_{\rm eff}$, fixed for all individuals within a data set, the Ising model accurately captures synchrony distributions (Figure 2). The optimal value of

 $N_{
m eff}=40$ is determined by scanning across $N_{
m eff}$ multiples of 5 to find which best captures the next order

- moment not fit by our maximum entropy setup across all individuals (Methods, Figure 6). For our
- particular preprocessing (Methods), we find that $N_{\rm eff}=40$ for individuals in the Cambridge Center for
- Ageing and Neuroscience (CamCAN) (Taylor et al., 2017) and the Human Connectome Project Aging
- (HCP) (Harms et al., 2018). For the UK Biobank (UKB) (Alfaro-Almagro et al., 2018), $N_{\rm eff}=30$
- ₈₉ performs best (Figure 6).
- Based on identified $N_{\rm eff}$ hyper-parameter values, brains act as if they have a few tens of functional
- units. If different preprocessing decisions are considered, such as atlas resolution, $N_{
 m eff}$ values are still
- within an order of magnitude. At the voxel-level (N=125,879), we obtain an $N_{\rm eff}$ value of 65 for
- ⁹³ CamCAN and 125 for HCP using the same procedure as for the Seitzman atlas (N = 300) considered in
- the previous paragraph (Figure S2). Future work will pinpoint how $N_{\rm eff}$ depends on preprocessing to
- enable a future study creating a physics-based parcellation of the brain.
- We also tried an alternative fitting strategy by fitting $N_{\rm eff}$ per individual rather than having the same
- value for all individuals in a respective data set. We show that individually fitted $N_{
 m eff}$ values trivially
- relate to λ as expected by theory (Figure S1). Moreover, individually fitted $N_{\rm eff}$ are not found to be
- related to global differences in anatomical brain connectivity (Figure S3).

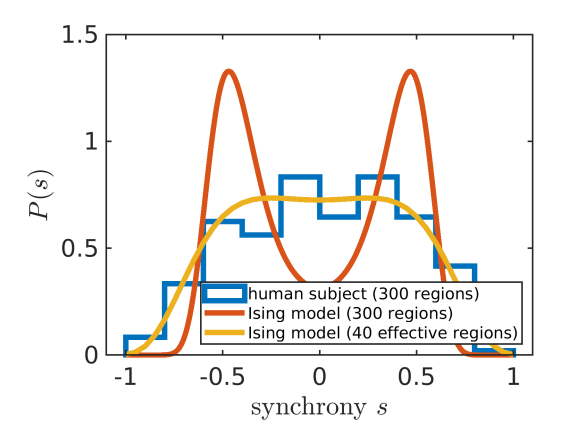


Figure 2. Adjusting the number of brain regions (N_{eff}) helps capture experiment. The modified Ising model with $N_{eff} = 40$ (yellow line) better captures the synchrony distribution (blue histogram) of an arbitrarily chosen individual in the Cambridge Centre for Ageing and Neuroscience data set (subject id: CC110045). The orange line corresponds to the Ising model with N equal to the number of regions in the Seitzman atlas (Seitzman et al., 2020).

The aging brain becomes functionally more segregated

With an appropriately determined $N_{\rm eff}$, we can accurately set the same synchrony threshold s^* for all individuals within a data set to calculate $P_{\rm seg}$. The value of s^* is set such that at the Ising model's critical point in connection strength λ , $P_{\rm seg}$ equals to 1/2 for the ideal synchrony distribution based on Ising model theory (Methods) . This enables $P_{\rm seg}$ comparisons across data sets that may have different $N_{\rm eff}$ values. For CamCAN and HCP, $s^*=0.33$ because $N_{\rm eff}=40$ for both data sets. For UKB, $s^*=0.36$ (Table S1).

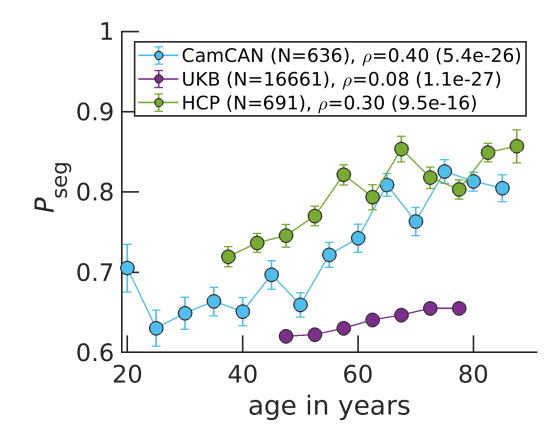


Figure 3. P_{seg} rises in aging brains across three data sets. Data points correspond to medians, while error bars correspond to standard errors for bins of 5 years. The variable ρ corresponds to the Spearman correlation coefficient between age and P_{seg} calculated over all N individuals, with the p-value in parenthesis.

Across the three publicly available data sets, we find that the balance shifts towards more segregation at older ages (Figure 3). Note that if we plotted $P_{\rm int}$ rather than $P_{\rm seg}$, Figure 3 would be horizontally flipped, where $P_{\rm int}$ goes from high to low values as a function of increasing age because $P_{\rm seg} + P_{\rm int} = 1$. There is large variation among subjects (Figure S4). However, the correlation between age and $P_{\rm seg}$ is significant with the largest coefficient being 0.40 for CamCAN, while the lowest being 0.08 for UKB. Discrepancies in study designs may explain correlation magnitude differences: CamCAN and HCP are designed to study healthy aging (Bookheimer et al., 2019; Shafto et al., 2014), while the goal of UKB is to identify early biomarkers for brain diseases (Sudlow et al., 2015).

younger, middle age and older individuals' P_{seg} (Figure S5). We also investigate how P_{seg} varies across

time for a given individual. In Figure S6, we show that the per individual P_{seg} standard deviations decrease across age for CamCAN and HCP individuals. Finally, we perform a multiple linear regression 124 with sex and handedness as additional covariates and show that age still strongly explains increasing 125 segregation (Table S2, S3 and S4; Figures S7, S8 and S9). Informed by the Ising model, increases in segregation result from network reorganization to more local 127 signaling because of weakened connection strength between regions. Interestingly, younger individuals 128 exhibit segregation behavior closer to the Ising model's critical point of connection strength (Figure S10). 129 At the critical point, we define $P_{\text{seg}} = 1/2$ (Methods) and find experimental P_{seg} values closer to 1/2 for younger individuals (Figure 3). Older individuals on the other hand, approach $P_{\text{seg}} = 1$ on average. This 131 limit corresponds to functionally uncoupled brain regions that are randomly activating. Our results support the critical brain hypothesis that healthy brains operate near a critical point (Beggs, 2022; Beggs & Plenz, 2003; Ponce-Alvarez, Kringelbach, & Deco, 2023; Tagliazucchi, Balenzuela, Fraiman, & Chialvo, 2012) and implicate aging as pushing brain dynamics further away from criticality.

Increasing segregation is not related to structural degradation

In the previous subsection, we discussed the disruption of the integration and segregation balance from the perspective of phase transitions in physics. Here, we explore the physiological mechanism underlying increasing segregation in the aging brain. We consecutively simulate the Ising model on a hypothetically degrading brain structure and show that random removal of edges yields qualitatively similar results to those of fMRI (Figure 4). Note that Figure 4 is horizontally flipped from those of P_{seg} (Figure 3) because average degree (relative number of edges) is on the x-axis. It is presumed that edges are lost as age increases. In Figure 4, edges are lost linearly in time, however, more complicated monotonic functions can be employed to yield a quantitative match with experimental data in Figure 3. We can also capture variability among individuals by assuming connection strengths within an individual are drawn from a distribution, rather than all being equal (Figure S11). In the supplement, we also demonstrate that similar qualitative trends are obtained when starting with other individuals' structures, regardless of their age (Figure S12).

Authors: R.M. Razban, B.B. Antal, K.A. Dill, L.R. Mujica-Parodi

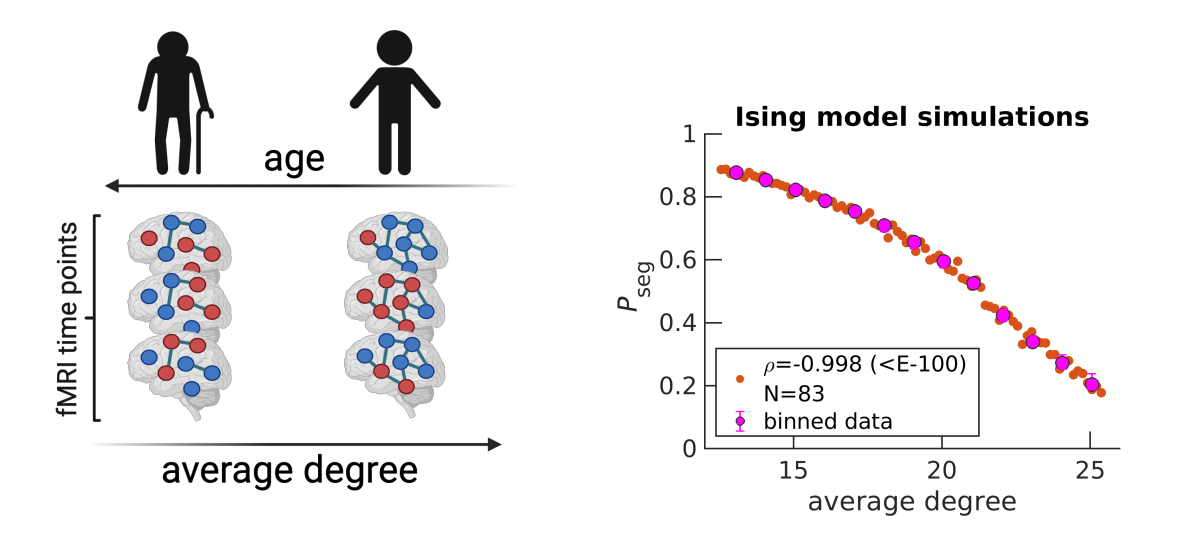


Figure 4. Simulating the random removal of edges results in P_{seg} increases. Five edges are randomly removed from a starting diffusion MRI structure (arbitrarily chosen UK Biobank individual, subject ID: 6025360, 51 years old), under the Harvard-Oxford atlas (64 regions). An Ising system is simulated with $N_{\text{eff}} = N = 64$ for the corresponding diffusion MRI structure. Spin states, denoted by dark blue and red node colors in the schematic, are recorded across 2500 time steps to calculate P_{seg} . Then, the entire procedure is repeated for the updated structure after edge removal, for a total of 83 times (Methods). Orange data points on the right plot correspond to individual Ising systems, where N reflects the total number. The variable ρ corresponds to the Spearman correlation coefficient calculated over all orange data points between average degree and P_{seg} , with the p-value in parenthesis. Magenta data points correspond to medians, while error bars correspond to upper and lower quartiles for bin sizes of one degree. The schematic on the left is created with Biorender.com.

We now begin to investigate possible mechanisms of connection degradation. First, we find that our 156 simulation is agnostic to the detailed mechanism of connection degeneration because connection strength is essentially modulated by the probability that a given edge exists (Figure S13). In other words, the simulation cannot inform whether connections are degraded based on some targeted property. Thus, we 159 turn to structural MRI and diffusion MRI data from UKB to investigate possible properties being degraded with age. In Figure S15, we confirm that white matter volume decreases as a function of adult age, as previously reported (Bethlehem et al., 2022; Lawrence et al., 2021; Lebel et al., 2012). However, 162 this decrease does not correspond to a loss of anatomical connections because we find that neither 163 average degree, average tract length nor average tract density monotonically decrease with age when analyzing diffusion MRI scans using the Q-Ball method (Figure S16). This seems to contradict previous 165 findings which report decreases (Betzel et al., 2014; Lim, Han, Uhlhaas, & Kaiser, 2015). However,

previous results employed the more simple diffusion tension imaging (DTI) method which is known to be

less accurate at performing tractography (Garyfallidis et al., 2014; Jones, Knösche, & Turner, 2013; Rokem et al., 2015). When rerunning our analysis for DTI, we can reproduce previously reported tract 169 properties' anticorrelations with age (Figure S16). We also investigate a graph property that captures polysynaptic connectivity called communicability (Andreotti et al., 2014; Estrada & Hatano, 2008; Seguin, Sporns, & Zalesky, 2023) and find that it also does not decrease age when using Q-Ball derived 172 tract density (Figure S17). 173 We propose that observed white matter volume reduction (Figure S15) and brain dynamics change 174 corresponds to less myelin covering axons as function of age. Despite rejecting anatomical connections 175 as a possible mechanism in the previous paragraph, it remains inconclusive whether myelin underlies 176 trends because we are not aware of such data being publicly available. Although axons are still physically present, myelin coverage disruption causes regions to no longer be functionally connected because signals do not arrive on time. Previously reported results from Myelin Water Imaging confirm reduction 179 in myelin at advanced ages (Arshad, Stanley, & Raz, 2016; Buyanova & Arsalidou, 2021). We also investigated whether degraded functional connections are likely to be longer than average with age, as previously reported for certain brain regions (Tomasi & Volkow, 2012). Although we indeed find that the average correlation of the 25% longest connections is slightly more strongly anticorrelated with age compared to the average correlation of the 25% shortest connections for CamCAN (Figure S18, left), we find the opposite trend for HCP (Figure S18, right). Thus, myelin reduction does not seem to have a stronger impact on longer connections and conclude that the loss of functional connections happens randomly with respect to length at the brain-wide scale.

DISCUSSION

We apply the mean field Ising model to physically quantify integration and segregation at the emergent scale of the whole brain. From resting-state fMRI scans across three publicly available data sets, we find that brain dynamics steadily becomes more segregated with age. Physically, aging leads to brain dynamics moving further away from its optimal balance at the critical point. Physiologically, analyses of white matter properties point to random functional connection losses due to myelin degeneration as the possible culprit for more segregated dynamics. This expands upon our previous work finding metabolic

dysfunction to underly brain aging (Weistuch et al., 2021), hinting that myelin may be especially

vulnerable to energy imbalances. 195 The Ising model and integration-segregation frameworks are considered as the simplest approaches to 196 capture dynamics in their respective fields. Thus, it is fitting to map segregated and integrated states in 197 neuroscience to disordered and ordered Ising model phases in physics, respectively. One general challenge in applying graph theory to MRI-level data is identifying what constitutes a node (DeFelipe, 199 2010; Lacy & Robinson, 2020; Seung, 2012; Sporns, 2010; Wig, Schlaggar, & Petersen, 2011; Yeo & 200 Eickhoff, 2016). We identify the best number of effective brain regions $N_{\rm eff}$ such that the Ising model accurately captures individuals' synchrony distributions across the corresponding data set, improving 202 upon our original application of the Ising model which lacked the $N_{\rm eff}$ hyper-parameter (Weistuch et al., 203 2021). Future work will utilize $N_{\rm eff}$ calculations to guide the creation of a parcellation in which brain regions are constrained to be physically independent based on their collective functional activity. 205 The field is inundated with integration and segregation metrics that have different aging trends. We go 206 beyond heuristic definitions, such as one that we previously proposed based on matrix decomposition 207 (Weistuch et al., 2021), by self-consistently defining the two states within the Ising model framework. This makes our metric mechanistically based on the connection strength between regions and further 209 stands out because P_{seg} and P_{int} are naturally at the emergent scale of the brain. We do not calculate a 210 local property and then average over nodes to yield a brain-wide value ((Wang et al., 2021)'s metric also has this advantage). In addition, P_{seg} and P_{int} are directly related because $P_{\text{seg}} + P_{\text{int}} = 1$. Most 212 integration and segregation metrics (Chan et al., 2014; Rubinov & Sporns, 2010; Tononi et al., 1994; 213 Wang et al., 2021) are not defined to be anti-correlated. This could be advantageous because greater complexity can be captured (Sporns, 2010). 215 Taken together, it is not surprising that P_{seg} and P_{int} results are not consistent with some previous aging 216 reports. For example, a property called system segregation, defined as the difference between inter- and 217 intra-correlations among modules, was found to decrease with age (Chan et al., 2014). Although most 218 report that segregation decreases with age, regardless of the specific metric (Chan et al., 2014; 219 Damoiseaux, 2017; King et al., 2018; Zhang et al., 2021) (see (Chen et al., 2021) for an exception), 220 integration trends are less clear. Global efficiency, taken from graph theory, was found to increase with age (Chan et al., 2014; Yao et al., 2019); however, others found different integration metrics decreasing

with age (Chong et al., 2019; Oschmann, Gawryluk, & Initiative, 2020; Zhang et al., 2021), consistent with results reported here.

The utility of the integration-segregation framework lies in its simplicity. However, its simplicity has led to various heuristic definitions that have qualitatively different aging trends. By physically defining integration and segregation based on connection strength between regions, we provide an interpretable foundation for more detailed studies going beyond the two-state approximation to investigate brain dynamics.

METHODS

230 fMRI preprocessing

We access three publicly available resting-state functional MRI data sets: Cambridge Centre for Ageing and Neuroscience (CamCAN) (Taylor et al., 2017), UK Biobank (UKB) (Alfaro-Almagro et al., 2018), and Human Connectome Project (HCP) (Harms et al., 2018). Acquisition details such as field strength and repetition time can be found in Table S5. Demographic details can be found in Table S6.

UKB and HCP fMRI data are accessed in preprocessed form (for details see (Alfaro-Almagro et al., 2018) and (Glasser et al., 2018, 2013), respectively). We preprocessed CamCAN data as done in our previous work (Weistuch et al., 2021). For all three data sets, the cleaned, voxel space time series are band-pass filtered to only include neuronal frequencies (0.01 to 0.1 Hz) and smoothed at a full width at half maximum of 5 mm. Finally, we parcellate into 300 regions of interest according to the Seitzman atlas (Seitzman et al., 2020). For our voxel-wide analysis presented in the Supporting Information, we do not perform parcellation and just consider gray mater voxels by masking.

Applying the Ising model requires the data to only take two possible values: -1 or 1. After performing
the preprocessing outlined in the previous paragraph, we binarize the continuous signal for a given region
based on the sign of the slope of subsequent time points (Weistuch et al., 2021). We previously showed
that such binarization still yields similar functional connectivities as that of the continuous data
(Weistuch et al., 2021).

Finally, we only consider brain scans that have the same number of measurements as the predominant number of individuals in the respective data set (Table S5). If the fitted connection strength parameter λ

is less than 0, reflecting a nonphysical value, we do not include that individual's brain scan in our analysis. In the HCP data set, we excluded individuals aged 90 years or older because their exact age, considered protected health information, is not available.

²⁵² Identifying the $N_{ m eff}$ hyper-parameter

In Figure 2, our maximum entropy fit (orange line) fails to qualitatively capture the synchrony distribution for an arbitrary individual. To rescue the fit, we replace N with $N_{\rm eff}$ (Equation S1). In the right plot of Figure 5, we demonstrate that a mean field Ising model with $N_{\rm eff}=40$ accurately captures the fourth moment of synchrony $\langle s^4 \rangle$ across all individuals in CamCAN preprocessed under the Seitzman atlas. Note that $N_{\rm eff}$ is not a parameter like Λ ; rather it is a hyper-parameter because it takes the same value across all individuals within the data set. $N_{\rm eff}$ is necessary because the Ising model systematically underestimates $\langle s^4 \rangle$ when $\Lambda > 0$ (left plot of Figure 5). Note that Λ corresponds to rescaling λ such that $\Lambda = 0$ is at the critical point (Equation S13).

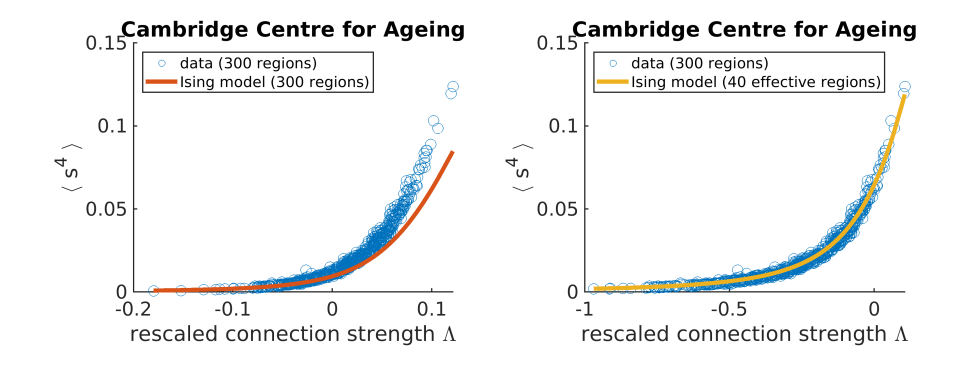


Figure 5. Adjusting the effective number of brain regions (N_{eff}) helps capture synchrony distributions' variances across individuals in the Cambridge Centre for Ageing data set. Each data point corresponds to an individual.

To identify $N_{\rm eff}=40$ as the best value, we perform a parameter scan over multiples of 5 and identify the $N_{\rm eff}$ at which the root mean square error (RMSE) between $\langle s^4 \rangle_{\rm exp}$ and $\langle s^4 \rangle_{\rm model}$ is minimized (Figure 6). We choose the fourth moment because it is the next order moment that our maximum entropy fit does not constrain. It is not the third moment because the distribution is assumed to be even as indicated by our prior (Equation S1).

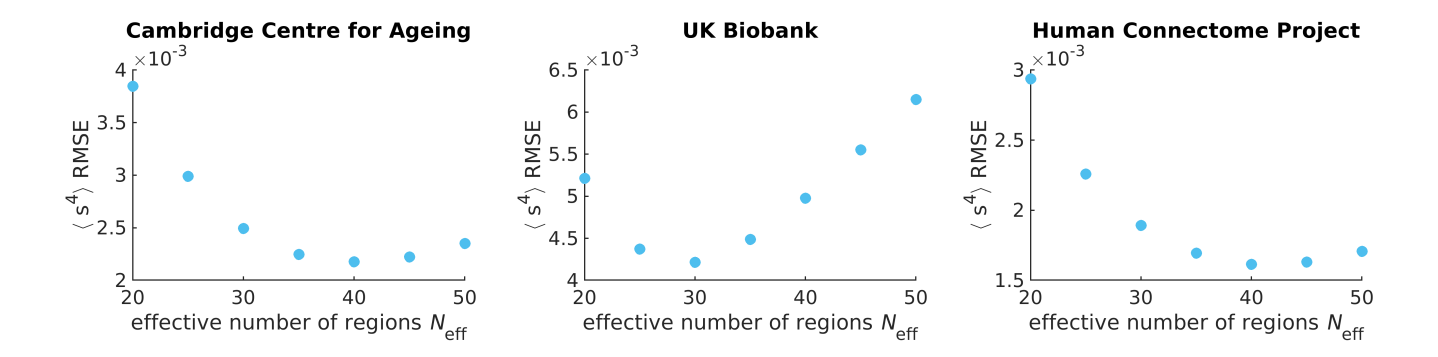


Figure 6. The effective number of regions N_{eff} is identified by minimizing the root mean square error (RMSE) of the fourth moment of synchrony between theory and experiment across all individuals. Each data point corresponds to the sum over all individuals' RMSEs in the respective data set. Note that the y-axis should be scaled by 10^{-3} .

271 Calculating P_{seg}

The probability of the brain network being in the segregated state is the sum over all microstates corresponding to the segregated state.

$$P_{\text{seg}} = \sum_{n = -N_{\text{eff}}s^*}^{N_{\text{eff}}s^*} P(n) \tag{1}$$

$$P_{\text{seg}} = \frac{1}{Z} \sum_{n = -N_{\text{eff}}s^*}^{N_{\text{eff}}s^*} {N_{\text{eff}} \choose (N_{\text{eff}} + n)/2} e^{\lambda n^2/N_{\text{eff}}^2}$$
(2)

In the second line, the mean field Ising model's P(n) is inserted (Equation S2). Z corresponds to the partition function and ensures that P(n) is normalized. The constant s^* is the synchrony threshold for which segregated and integrated microstates are delineated. We set s^* such that $P_{\text{seg}} = 1/2$ when $\Lambda = 0$ according to theory. More specifically, we numerically calculate $P_{\text{seg}}(\Lambda = 0)$ for a given N_{eff} and extrapolate to find s^* (Figure S19). Proper calibration ensures that the theory is accurate and enables apples to apples P_{seg} comparisons across data sets with different N_{eff} . The list of s^* values for the three publicly available data sets studied can be found in Table S1.

281 Ising model simulation

Authors: R.M. Razban, B.B. Antal, K.A. Dill, L.R. Mujica-Parodi

```
We simulate the Ising model on an initial structure informed by diffusion MRI under the Harvard-Oxford
   atlas (Makris et al., 2006) (64 regions) for an arbitrarily chosen UK Biobank individual (subject ID:
283
   6025360). If no edge exists between two regions, then the regions are uncoupled. If an edge does exist,
284
   then regions i and j are coupled and contribute \lambda * \sigma_i * \sigma_j to the system's energy; where \lambda corresponds to
285
   the connection strength and \sigma corresponds to the spin state of the corresponding region (-1 or 1). Under
   the standard notation of the Ising model, \lambda = J/T, where J corresponds to the coupling constant and T
287
   is the temperature of the bath. The starting \lambda is set to 34.4, which is above \lambda's critical point (starting
   P_{\rm seg} \approx 0.2). By definition, N_{\rm eff} = N = 64 in the simulations. Based on atlas resolution, simulating the
   Harvard-Oxford atlas provides an N_{
m eff} similar to those found for the experimental data (N_{
m eff}=40 for
   CamCAN and HCP; N_{\rm eff}=30 for UKB).
291
      The simulation for a given structure starts by randomly assigning the 64 nodes up or down spins. Then,
   for each time step, we attempt 10 spin flips 64 times, for a total of 2500 time steps. Spin flips are
293
   accepted according to the Metropolis-Hastings algorithm (Metropolis, Rosenbluth, Rosenbluth, Teller, &
294
   Teller, 1953). The exact number of spin flip attempts or total time points does not matter, as long as
295
   equilibrium is reached. For example, we find that for \lambda values larger than those presented in the text,
   synchrony distributions become asymmetric and exhibit only one of the two peaks corresponding to the
297
   integrated state because of the high kinetic barrier of going from all down spins to all up spins.
      Although the starting structure is informed by diffusion MRI, resulting structures after computational
   edge removals are based on the posited removal strategy. Edges informed by dMRI are undirected and
300
   removal maintains undirectedness. Effectively two times as many edges are removed because both
301
   forward and backward edges are concurrently eliminated. In Figure S14, we demonstrate how synchrony
   distributions change as edges are computationally removed for a UK Biobank individual (subject ID:
   6025360), with a starting \lambda = 34.4.
304
      We also investigate other individuals' structures in the UK Biobank to test the robustness of our
305
   qualitative results. We arbitrarily chose the following six individuals to widely sample different ages;
   subject IDs: 6025360 (51y), 4712851 (57y), 3081886 (61y), 1471888 (65y), 4380337 (72y), and
307
   1003054 (74y) (Figure S12). To ensure that the starting \lambda are comparable despite differing in the
308
   probability that two regions are connected (p_{\text{edge}}), we set \lambda_0 = 86.0 for all simulations such that
   \lambda = \lambda_0 * p_{\text{edge}}. For example, for subject ID: 6025360, p_{\text{edge}} = 0.40, thus the starting \lambda = 34.4.
```

Authors: R.M. Razban, B.B. Antal, K.A. Dill, L.R. Mujica-Parodi

311 Diffusion MRI analysis

- Diffusion MRI processing to obtain structural information such as tract length and streamline count,
- which we call tract density, is outlined in our previous work (Razban, Pachter, Dill, & Mujica-Parodi,
- 2023). Briefly, we take preprocessed dMRI scans from the UK Biobank (Sudlow et al., 2015) and
- calculate connectivity matrices using the Diffusion Imaging in Python software (Garyfallidis et al.,
- ³¹⁶ 2014). We input the Talairach atlas (Lancaster et al., 2000) to distinguish between white and gray matter.
- We perform deterministic tractography and reconstruct the orientation distribution function using
- ³¹⁸ Constant Solid Angle (Q-Ball) with a spherical harmonic order of 6 (Aganj et al., 2010). For Figure S16,
- we also do reconstruction using diffusion tensor imaging (Garyfallidis et al., 2014). To generate the
- starting structure for Ising model simulations, we input the Harvard-Oxford atlas for tractography
- because it parcellates the brain into fewer regions, making it more computationally tractable to carry out
- $N_{\rm eff}$ simulations and closer to $N_{\rm eff}$ values found for experimental data.

323 Code and data availability

- Scripts necessary to reproduce figures and conclusions reached in the text can be found at
- github.com/rrazban/2state_brain. Please refer to the respective publicly available data set to access
- previously published data (CamCAN, UKB and HCP) (Alfaro-Almagro et al., 2018; Harms et al., 2018;
- 327 Taylor et al., 2017).

ACKNOWLEDGMENTS

- We thank Ying-Jen Yang, Anthony Chesebro, Charles Kocher, Jonathan Pachter and Lakshman Verma
- for insightful discussions. The research described in this paper is funded by the White House Brain
- Research Through Advancing Innovative Technologies (BRAIN) Initiative (NSFNCS-FR 1926781 to
- L.R.M.-P. and K.A.D.) and the Stony Brook University Laufer Center for Physical and Quantitative
- Biology (K.A.D.).
- Data collection and sharing for this project was provided by the Cambridge Centre for Ageing and
- Neuroscience (CamCAN). CamCAN funding was provided by the UK Biotechnology and Biological
- Sciences Research Council (grant number BB/H008217/1), together with support from the UK Medical
- Research Council and University of Cambridge, UK.

This research has been conducted using the UK Biobank Resource under Application Number 37462.

Research reported in this publication was supported by the National Institute On Aging of the National

Institutes of Health under Award Number U01AG052564 and by funds provided by the McDonnell

³⁴⁰ Center for Systems Neuroscience at Washington University in St. Louis. The HCP-Aging 2.0 Release

data used in this report came from DOI: 10.15154/1520707. The HCP data repository grows and changes

over time. The HCP data used in this report came from NIMH Data Archive DOI:10.15154/1526427.

344

REFERENCES

345

350

Aganj, I., Lenglet, C., Sapiro, G., Yacoub, E., Ugurbil, K., & Harel, N. (2010). Reconstruction of the orientation distribution

function in single-and multiple-shell q-ball imaging within constant solid angle. Magnetic resonance in medicine, 64(2),

₃₄₈ 554–566.

Alfaro-Almagro, F., Jenkinson, M., Bangerter, N. K., Andersson, J. L., Griffanti, L., Douaud, G., ... others (2018). Image

processing and quality control for the first 10,000 brain imaging datasets from uk biobank. *Neuroimage*, 166, 400–424.

Andreotti, J., Jann, K., Melie-Garcia, L., Giezendanner, S., Abela, E., Wiest, R., ... Federspiel, A. (2014). Validation of

network communicability metrics for the analysis of brain structural networks. *PloS one*, 9(12), e115503.

Arshad, M., Stanley, J. A., & Raz, N. (2016). Adult age differences in subcortical myelin content are consistent with

protracted myelination and unrelated to diffusion tensor imaging indices. *Neuroimage*, 143, 26–39.

Beggs, J. M. (2022). Addressing skepticism of the critical brain hypothesis. Frontiers in Computational Neuroscience, 16.

Beggs, J. M., & Plenz, D. (2003). Neuronal avalanches in neocortical circuits. *Journal of neuroscience*, 23(35),

11167–11177.

Bermejo-Pareja, F., Benito-León, J., Vega, S., Medrano, M., Roman, G. C., in Central Spain (NEDICES) Study Group,

N. D., et al. (2008). Incidence and subtypes of dementia in three elderly populations of central spain. *Journal of the*

neurological sciences, 264(1-2), 63–72.

Bethlehem, R. A., Seidlitz, J., White, S. R., Vogel, J. W., Anderson, K. M., Adamson, C., ... others (2022). Brain charts for

the human lifespan. *Nature*, 604(7906), 525–533.

- Betzel, R. F., Byrge, L., He, Y., Goñi, J., Zuo, X.-N., & Sporns, O. (2014). Changes in structural and functional connectivity among resting-state networks across the human lifespan. *Neuroimage*, *102*, 345–357.
- Bookheimer, S. Y., Salat, D. H., Terpstra, M., Ances, B. M., Barch, D. M., Buckner, R. L., ... others (2019). The lifespan human connectome project in aging: an overview. *Neuroimage*, *185*, 335–348.
- Bullmore, E., & Sporns, O. (2012). The economy of brain network organization. *Nature reviews neuroscience*, *13*(5), 336–349.
- Buyanova, I. S., & Arsalidou, M. (2021). Cerebral white matter myelination and relations to age, gender, and cognition: A selective review. *Frontiers in human neuroscience*, *15*, 662031.
- Chan, M. Y., Park, D. C., Savalia, N. K., Petersen, S. E., & Wig, G. S. (2014). Decreased segregation of brain systems across the healthy adult lifespan. *Proceedings of the National Academy of Sciences*, *111*(46), E4997–E5006.
- Chen, X., Necus, J., Peraza, L. R., Mehraram, R., Wang, Y., O'Brien, J. T., ... Taylor, J.-P. (2021). The functional brain favours segregated modular connectivity at old age unless affected by neurodegeneration. *Communications biology*, *4*(1), 973.
- Chong, J. S. X., Ng, K. K., Tandi, J., Wang, C., Poh, J.-H., Lo, J. C., ... Zhou, J. H. (2019). Longitudinal changes in the cerebral cortex functional organization of healthy elderly. *Journal of Neuroscience*, *39*(28), 5534–5550.
- Cohen, J. R., & D'Esposito, M. (2016). The segregation and integration of distinct brain networks and their relationship to cognition. *Journal of Neuroscience*, *36*(48), 12083–12094.
- Damoiseaux, J. S. (2017). Effects of aging on functional and structural brain connectivity. *Neuroimage*, 160, 32–40.
- Deco, G., Tononi, G., Boly, M., & Kringelbach, M. L. (2015). Rethinking segregation and integration: contributions of whole-brain modelling. *Nature Reviews Neuroscience*, *16*(7), 430–439.
- DeFelipe, J. (2010). From the connectome to the synaptome: an epic love story. *science*, 330(6008), 1198–1201.
- Dill, K., & Bromberg, S. (2012). *Molecular driving forces: statistical thermodynamics in biology, chemistry, physics, and*nanoscience. Garland Science.
- Estrada, E., & Hatano, N. (2008). Communicability in complex networks. *Physical Review E*, 77(3), 036111.

- Friedli, S., & Velenik, Y. (2017). *Statistical mechanics of lattice systems: a concrete mathematical introduction*. Cambridge
 University Press.
- Friston, K. J. (2009). Modalities, modes, and models in functional neuroimaging. Science, 326(5951), 399-403.
- Garyfallidis, E., Brett, M., Amirbekian, B., Rokem, A., Van Der Walt, S., Descoteaux, M., ... Contributors, D. (2014).
- Dipy, a library for the analysis of diffusion mri data. Frontiers in neuroinformatics, 8, 8.
- Glasser, M. F., Coalson, T. S., Bijsterbosch, J. D., Harrison, S. J., Harms, M. P., Anticevic, A., ... Smith, S. M. (2018).
- Using temporal ica to selectively remove global noise while preserving global signal in functional mri data. *Neuroimage*,
- *181*, 692–717.
- Glasser, M. F., Sotiropoulos, S. N., Wilson, J. A., Coalson, T. S., Fischl, B., Andersson, J. L., ... others (2013). The minimal preprocessing pipelines for the human connectome project. *Neuroimage*, 80, 105–124.
- Harms, M. P., Somerville, L. H., Ances, B. M., Andersson, J., Barch, D. M., Bastiani, M., ... others (2018). Extending the
- human connectome project across ages: Imaging protocols for the lifespan development and aging projects. *Neuroimage*,
- 183, 972–984.
- Jones, D. K., Knösche, T. R., & Turner, R. (2013). White matter integrity, fiber count, and other fallacies: the do's and don'ts of diffusion mri. *Neuroimage*, 73, 239–254.
- Kennedy, B. K., Berger, S. L., Brunet, A., Campisi, J., Cuervo, A. M., Epel, E. S., ... others (2014). Geroscience: linking aging to chronic disease. *Cell*, 159(4), 709–713.
- King, B. R., Van Ruitenbeek, P., Leunissen, I., Cuypers, K., Heise, K.-F., Santos Monteiro, T., ... others (2018).
- Age-related declines in motor performance are associated with decreased segregation of large-scale resting state brain
- networks. *Cerebral Cortex*, 28(12), 4390–4402.
- Kochmański, M., Paszkiewicz, T., & Wolski, S. (2013). Curie-weiss magnet—a simple model of phase transition.
- European Journal of Physics, 34(6), 1555.
- Lacy, T. C., & Robinson, P. A. (2020). Effects of parcellation and threshold on brainconnectivity measures. *Plos one*,
- 410 15(10), e0239717.

- Lancaster, J. L., Woldorff, M. G., Parsons, L. M., Liotti, M., Freitas, C. S., Rainey, L., ... Fox, P. T. (2000). Automated talairach atlas labels for functional brain mapping. *Human brain mapping*, *10*(3), 120–131.
- Landau, L. D. (1937). On the theory of phase transitions. I. Zhurnal Eksperimental'noi i Teoreticheskoi Fiziki, 11, 19.
- Lawrence, K. E., Nabulsi, L., Santhalingam, V., Abaryan, Z., Villalon-Reina, J. E., Nir, T. M., ... others (2021). Age and sex effects on advanced white matter microstructure measures in 15,628 older adults: a uk biobank study. *Brain Imaging*and Behavior, 15(6), 2813–2823.
- Lebel, C., Gee, M., Camicioli, R., Wieler, M., Martin, W., & Beaulieu, C. (2012). Diffusion tensor imaging of white matter tract evolution over the lifespan. *Neuroimage*, *60*(1), 340–352.
- Lim, S., Han, C. E., Uhlhaas, P. J., & Kaiser, M. (2015). Preferential detachment during human brain development: age-and sex-specific structural connectivity in diffusion tensor imaging (dti) data. *Cerebral Cortex*, 25(6), 1477–1489.
- Makris, N., Goldstein, J. M., Kennedy, D., Hodge, S. M., Caviness, V. S., Faraone, S. V., ... Seidman, L. J. (2006).

 Decreased volume of left and total anterior insular lobule in schizophrenia. *Schizophrenia research*, 83(2-3), 155–171.
- Manza, P., Wiers, C. E., Shokri-Kojori, E., Kroll, D., Feldman, D., Schwandt, M., ... Volkow, N. D. (2020). Brain network segregation and glucose energy utilization: relevance for age-related differences in cognitive function. *Cerebral Cortex*, 30(11), 5930–5942.
- Metropolis, N., Rosenbluth, A. W., Rosenbluth, M. N., Teller, A. H., & Teller, E. (1953). Equation of state calculations by fast computing machines. *The journal of chemical physics*, *21*(6), 1087–1092.
- Onoda, K., & Yamaguchi, S. (2013). Small-worldness and modularity of the resting-state functional brain network decrease with aging. *Neuroscience letters*, *556*, 104–108.
- Oschmann, M., Gawryluk, J. R., & Initiative, A. D. N. (2020). A longitudinal study of changes in resting-state functional magnetic resonance imaging functional connectivity networks during healthy aging. *Brain Connectivity*, *10*(7), 377–384.
- Ponce-Alvarez, A., Kringelbach, M. L., & Deco, G. (2023). Critical scaling of whole-brain resting-state dynamics.
- *Communications Biology*, *6*(1), 627.
- Raichle, M. E. (2006). The brain's dark energy. *Science*, 314(5803), 1249–1250.

- Razban, R. M., Pachter, J. A., Dill, K. A., & Mujica-Parodi, L. R. (2023). Early path dominance as a principle for
- neurodevelopment. Proceedings of the National Academy of Sciences, 120(16), e2218007120.
- Rokem, A., Yeatman, J. D., Pestilli, F., Kay, K. N., Mezer, A., Van Der Walt, S., & Wandell, B. A. (2015). Evaluating the
- accuracy of diffusion mri models in white matter. *PloS one*, *10*(4), e0123272.
- Rubinov, M., & Sporns, O. (2010). Complex network measures of brain connectivity: uses and interpretations. *Neuroimage*,
- 52(3), 1059–1069.
- Schneidman, E., Berry, M. J., Segev, R., & Bialek, W. (2006). Weak pairwise correlations imply strongly correlated network
- states in a neural population. *Nature*, 440(7087), 1007–1012.
- Seguin, C., Sporns, O., & Zalesky, A. (2023). Brain network communication: concepts, models and applications. *Nature*
- reviews neuroscience, 24(9), 557–574.
- Seitzman, B. A., Gratton, C., Marek, S., Raut, R. V., Dosenbach, N. U., Schlaggar, B. L., ... Greene, D. J. (2020). A set of
- functionally-defined brain regions with improved representation of the subcortex and cerebellum. *Neuroimage*, 206,
- 447 116290.
- Seung, S. (2012). Connectome: How the brain's wiring makes us who we are. HMH.
- Shafto, M. A., Tyler, L. K., Dixon, M., Taylor, J. R., Rowe, J. B., Cusack, R., ... others (2014). The cambridge centre for
- ageing and neuroscience (cam-can) study protocol: a cross-sectional, lifespan, multidisciplinary examination of healthy
- cognitive ageing. *BMC neurology*, *14*, 1–25.
- Sporns, O. (2010). *Networks of the brain*. MIT press.
- Sporns, O. (2013). Network attributes for segregation and integration in the human brain. *Current opinion in neurobiology*,
- 454 *23*(2), 162–171.
- Sudlow, C., Gallacher, J., Allen, N., Beral, V., Burton, P., Danesh, J., ... others (2015). Uk biobank: an open access resource
- for identifying the causes of a wide range of complex diseases of middle and old age. *PLoS medicine*, 12(3), e1001779.
- ⁴⁵⁷ Tagliazucchi, E., Balenzuela, P., Fraiman, D., & Chialvo, D. R. (2012). Criticality in large-scale brain fmri dynamics
- unveiled by a novel point process analysis. Frontiers in physiology, 3, 15.
- Taylor, J. R., Williams, N., Cusack, R., Auer, T., Shafto, M. A., Dixon, M., ... others (2017). The cambridge centre for

- ageing and neuroscience (cam-can) data repository: Structural and functional mri, meg, and cognitive data from a cross-sectional adult lifespan sample. *Neuroimage*, *144*, 262–269.
- Tomasi, D., & Volkow, N. D. (2012). Aging and functional brain networks. *Molecular psychiatry*, 17(5), 549–558.
- Tononi, G., Sporns, O., & Edelman, G. M. (1994). A measure for brain complexity: relating functional segregation and integration in the nervous system. *Proceedings of the National Academy of Sciences*, *91*(11), 5033–5037.
- Wang, R., Liu, M., Cheng, X., Wu, Y., Hildebrandt, A., & Zhou, C. (2021). Segregation, integration, and balance of large-scale resting brain networks configure different cognitive abilities. *Proceedings of the National Academy of*
- *Sciences*, 118(23), e2022288118.
- Weistuch, C., Mujica-Parodi, L. R., Razban, R. M., Antal, B., van Nieuwenhuizen, H., Amgalan, A., & Dill, K. A. (2021).
- Metabolism modulates network synchrony in the aging brain. *Proceedings of the national academy of sciences*, 118(40),
- e2025727118.
- Wig, G. S. (2017). Segregated systems of human brain networks. Trends in cognitive sciences, 21(12), 981–996.
- Wig, G. S., Schlaggar, B. L., & Petersen, S. E. (2011). Concepts and principles in the analysis of brain networks. *Annals of*the New York Academy of Sciences, 1224(1), 126–146.
- Yao, Z., Zou, Y., Zheng, W., Zhang, Z., Li, Y., Yu, Y., ... others (2019). Structural alterations of the brain preceded functional alterations in major depressive disorder patients: Evidence from multimodal connectivity. *Journal of affective disorders*, 253, 107–117.
- Yeo, B. T., & Eickhoff, S. B. (2016). A modern map of the human cerebral cortex. *Nature*, 536(7615), 152–154.
- Zhang, Y., Wang, Y., Chen, N., Guo, M., Wang, X., Chen, G., ... others (2021). Age-associated differences of modules and hubs in brain functional networks. *Frontiers in aging neuroscience*, *12*, 607445.

Authors: R.M. Razban, B.B. Antal, K.A. Dill, L.R. Mujica-Parodi

SUPPORTING INFORMATION

- Deriving the Ising model with $N_{
 m eff}$
- Many have derived the probability distribution of the mean field Ising model, otherwise known as the
- fully connected or Curie-Weiss Ising model (Friedli & Velenik, 2017; Kochmański, Paszkiewicz, &
- Wolski, 2013; Weistuch et al., 2021). Here, we demonstrate how to introduce N_{eff} in a Maximum Entropy
- framework. The tricky part is that $N_{
 m eff}$ defines the state space over which the probability distribution is
- summed. 485

494

- Adding a global pairwise correlation constraint, we obtain the following Lagrangian function \mathcal{L} over 486
- the net displacement of spin states $n = \sum_{i=1}^{N_{\text{eff}}} \sigma_i$, where σ_i can take a value of 1 or -1.

$$\mathcal{L} = \sum_{n}^{N_{\text{eff}}} P(n) \ln \frac{P(n)}{q(n)} + \alpha \left(\sum_{n}^{N_{\text{eff}}} P(n) - 1 \right) + \lambda \left(\frac{1}{(N_{\text{eff}})^2} \sum_{n}^{N_{\text{eff}}} n^2 P(n) - \langle s^2 \rangle_{\text{exp}} \right)$$
(S1)

P is the probability distribution. q corresponds to the prior and is set to the binomial distribution $\binom{N}{(N+n)/2}2^{-N}$, where the binomial coefficient captures the number of ways individual spins can organize for a given n. α and λ correspond to the Lagrange multipliers that enforce the constraints that the probability distribution is normalized and the mean pairwise correlation equals $\langle s^2 \rangle$, respectively. The variable s corresponds to the synchrony, or commonly referred to as the magnetization in ferromagnetic applications, and is limited to vary from -1 to 1 because $n = N_{\text{eff}}s$. This is the reason N does not have to

Maximizing the Lagrangian function (Equation S1) with respect to P, we obtain the following distribution:

be the same for $\langle s^2 \rangle_{\text{exp}}$ and $\langle s^2 \rangle_{\text{model}}$; $\langle s^2 \rangle$ is always bounded between -1 and 1.

$$P(n) = Z^{-1} \binom{N_{\text{eff}}}{(N_{\text{eff}} + n)/2} e^{\lambda n^2 / N_{\text{eff}}^2}$$
(S2)

$$P(n) = Z^{-1} \binom{N_{\text{eff}}}{(N_{\text{eff}} + n)/2} e^{\lambda n^2 / N_{\text{eff}}^2}$$

$$P(s) = Z^{-1} \binom{N_{\text{eff}}}{N_{\text{eff}}(1+s)/2} e^{\lambda s^2}$$
(S2)

Z corresponds to the partition function and ensures that P is normalized. The α Lagrange multiplier is 497 not present in the final expression because it is subsumed by Z.

499 Ising model phase transitions

The Landau model is a general formulation to study phase transitions (Dill & Bromberg, 2012; Landau, 1937). It takes the following form,

$$F(T) = A(T - T_c)\eta^2 + B\eta^4 \tag{S4}$$

 η corresponds to the order parameter. F is the free energy and can be expressed as the probability for being in microstate i by the following relationship $F_i = k_b T \ln P_i$. T is the temperature and T_c corresponds to the critical temperature at which a second-order phase transition occurs. A and B are constants.

Here, we will express the Ising model's probability distribution (Equation S3) in terms of the Landau formalism (Equation S4) by approximating the binomial coefficient as an exponential to order (s^4) . For brevity, we will write N to represent N_{eff} . First, we use Stirling's approximation to expand the binomial coefficient.

$$\binom{N}{N(1+s)/2} = N! \left[(N(1+s)/2)! \left(N(1-s)/2 \right)! \right]^{-1}$$

$$\approx N^N \left[\left(\frac{N(1+s)}{2} \right) \frac{N(1+s)}{2} \left(\frac{N(1-s)}{2} \right) \frac{N(1-s)}{2} \right]^{-1}$$

$$= N^N \left[\left(\frac{N}{2} \right) \frac{N(1+s)}{2} (1+s) \frac{N(1+s)}{2} \left(\frac{N}{2} \right) \frac{N(1-s)}{2} (1-s) \frac{N(1-s)}{2} \right]^{-1}$$
(S5)

$$= N^{N} \left[\left(\frac{N}{2} \right)^{N} \left([1+s][1-s] \right)^{N/2} \left(\frac{1+s}{1-s} \right)^{Ns/2} \right]^{-1}$$
 (S8)

$$=2^{N} \left[\frac{1}{1-s^2} \left(\frac{1-s}{1+s} \right)^s \right]^{N/2}$$
 (S9)

To make further headway, we assume that s approaches 0 and expand Equation S9 to order s^4 .

Authors: R.M. Razban, B.B. Antal, K.A. Dill, L.R. Mujica-Parodi

$$\binom{N}{N(1+s)/2} \approx 2^N \left[1 - s^2 - \frac{1}{3} s^4 \right]^{N/2} \tag{S10}$$

Next, we assume N is large and express the term under the brackets as an exponential.

$$\binom{N}{N(1+s)/2} \approx 2^N \exp\left[-\frac{N}{2}s^2 - \frac{N}{12}s^4\right] \tag{S11}$$

We can insert our approximate expression for the binomial coefficient back into P(s) (Equation S3) and obtain,

$$P(s) \approx Z^{-1} 2^N \exp\left[\left(\lambda - \frac{N}{2}\right) s^2 - \frac{N}{12} s^4\right]$$
 (S12)

Note that Equation S12 (after transforming into free energy space) maps onto Landau theory (Equation S4). s corresponds to the order parameter and $\lambda_c = N/2$. At $\lambda = \lambda_c$, P(s) switches from unimodal to bimodal, corresponding to a second order phase transition. We report a rescaled version of λ called Λ in Figure 5 and in other places in the Supporting Information to easily gauge how far an individual's connection strength is from the critical point.

$$\Lambda = \frac{\lambda - \lambda_{\text{critical}}}{\lambda_{\text{critical}}} \tag{S13}$$

517 Alternative $N_{ m eff}$ fitting approach

Rather than choose one $N_{\rm eff}$ for all individuals in the data set as done in the main text, we could fit $N_{\rm eff}$ for each individual. Figure S1 demonstrates that such a procedure results in $N_{\rm eff}$ values that are highly linearly related with λ . In other words, more precise $N_{\rm eff}$ fits do not provide any more insight than maximum entropy fits of λ for all individuals in a data set under one optimal $N_{\rm eff}$.

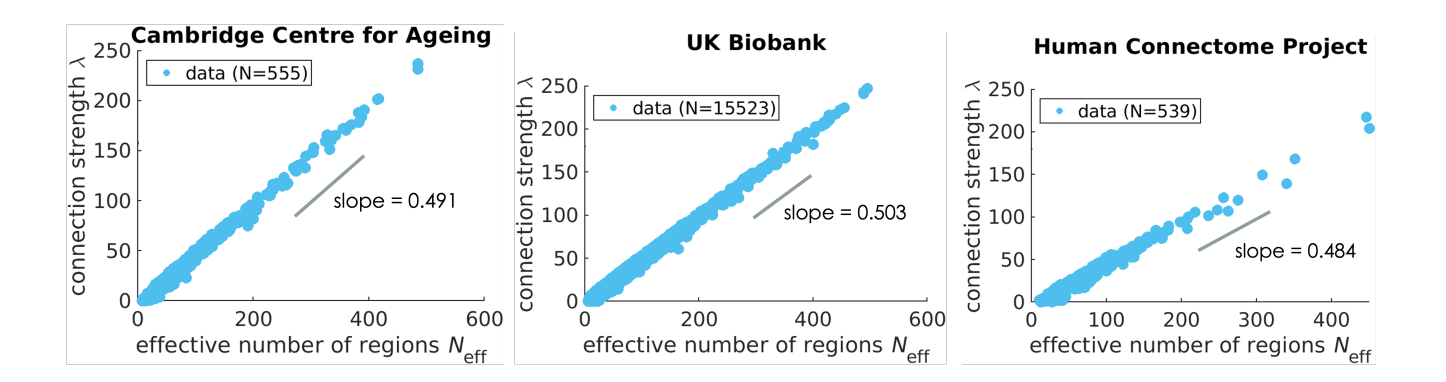


Figure S1. Treating $N_{\rm eff}$ as a parameter and fitting it per individual yields a strong correlation with λ . Each point reflects an individual brain scan and N reflects the total number analyzed. The value of the slope corresponds to that of the best-fit line for the data and is close to the predicted value of 0.5 (Equation S15). N is smaller than that of Figure 3 because some scans failed to have a minimum $\langle s^4 \rangle$ RMSE within the explored bounds of $N_{\rm eff}$ (4-500) or λ values were nonphysical by being less than 0.

The $N_{\rm eff}$ - λ relationship can be reasoned from the analytical expression for P(s) (Equation S12). When $\Lambda < 0$, which many individuals satisfy (Figure S10), P(s) is well-approximated as a Gaussian.

$$P(s) \propto \exp\left[\left(\lambda - \frac{N_{\rm eff}}{2}\right)s^2\right]$$
 (S14)

Thus, the analytical form for $\langle s^2 \rangle$ is:

$$\langle s^2 \rangle = -\frac{1}{2\lambda - N_{\text{eff}}} \tag{S15}$$

Since λ is fit in the Maximum Entropy framework to exactly match $\langle s^2 \rangle$, Equation S15 indicates that a larger $N_{\rm eff}$ requires a larger λ for a fixed $\langle s^2 \rangle$. Indeed, we find in Figure S1 that the best fit line of the $N_{\rm eff}$ - λ relationship has an approximate slope of 0.5, in agreement with Equation S15.

531 More supporting information

Table S1. Data set values for P_{seg} calculations under our particular fMRI preprocessing procedure (Methods).

532

Data set	effective number of regions $N_{\rm eff}$	synchrony threshold s^*
Cambridge Centre for Ageing	40	0.334
UK Biobank	30	0.357
Human Connectome Project	40	0.334

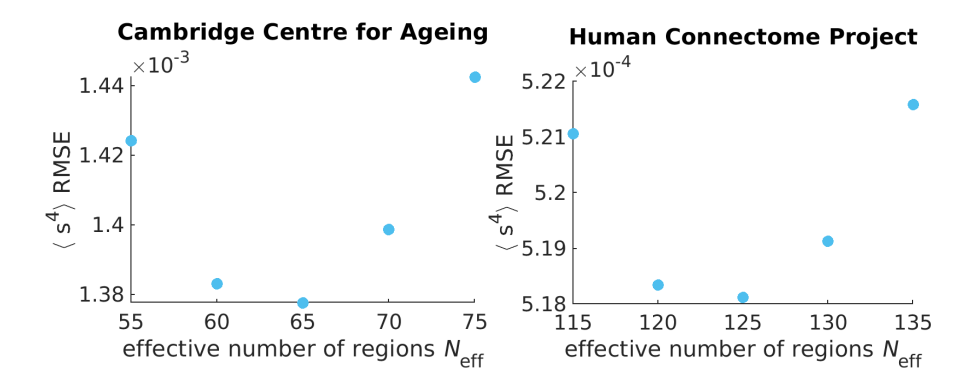


Figure S2. Identifying the effective number of regions N_{eff} for brain scans processed at the voxel-level. Each data point corresponds to the sum over all individuals' RMSEs in the respective data set.

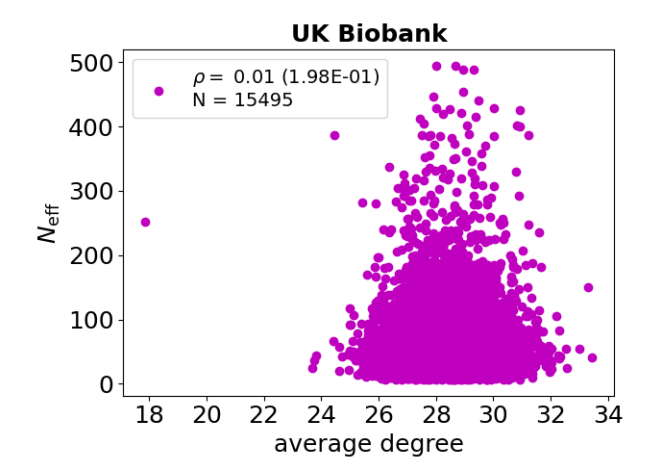


Figure S3. Individually fitted $N_{\rm eff}$ values from Figure S1 are not related to the average number of white matter tracts per brain region (average degree) as
determined by diffusion MRI. The Q-Ball tractography method is used to analyze diffusion MRI scans (Methods). Data points correspond to individuals.

The variable ρ corresponds to the Spearman correlation coefficient between average degree and $N_{\rm eff}$ calculated over all N individuals, with the p-value in
parenthesis.

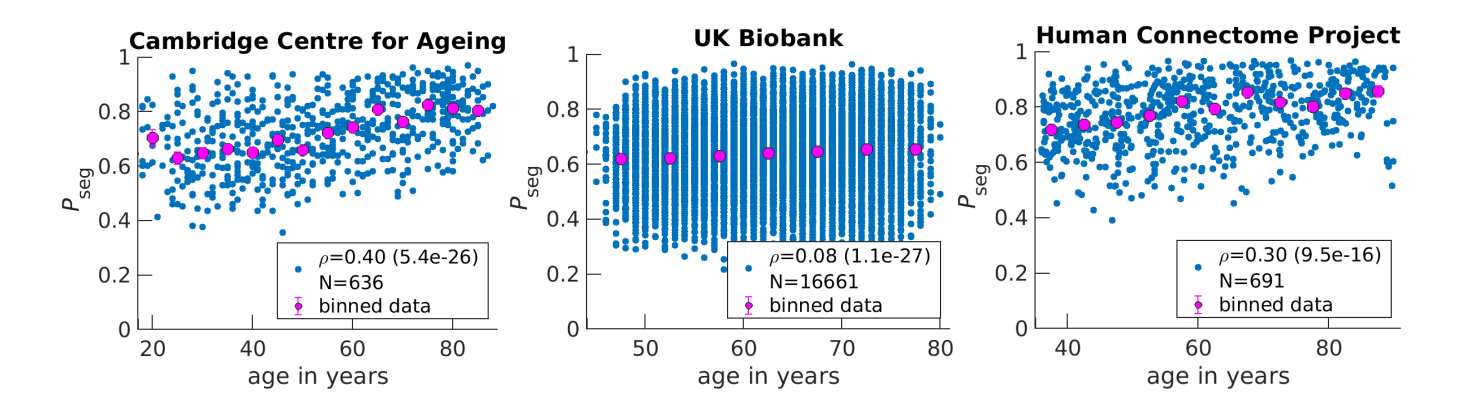


Figure S4. P_{seg} rises on average in aging brains but varies greatly among individuals with the same age. Blue data points correspond to individuals. The variable ρ corresponds to the Spearman correlation coefficient between age and P_{seg} calculated over all N individuals, with the p-value in parenthesis. Magenta points are the exact same data points presented in Figure 3 for the corresponding data set. Note that the corresponding error bars are not visible in these plots.

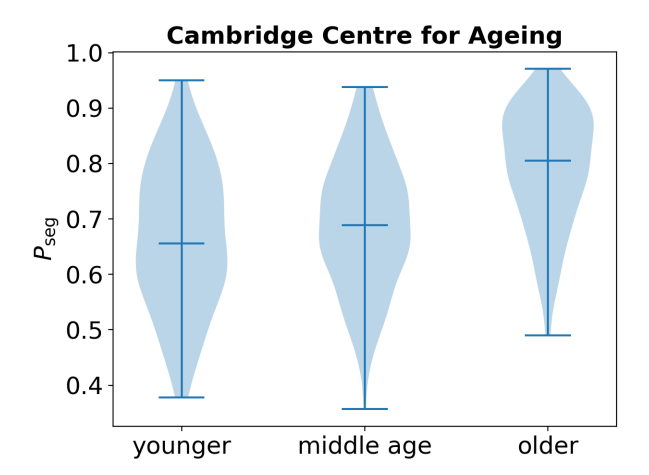


Figure S5. P_{seg} rises in aging brains across three Cambridge Centre for Ageing and Neuroscience age groups. Violin plots are presented, where middle horizontal lines correspond to medians while lower and upper lines correspond to minimum and maximum values, respectively. Younger individuals are those less than 35 years old (N=117); middle age, 40-60y (N=187); older, above 65y (N=209).

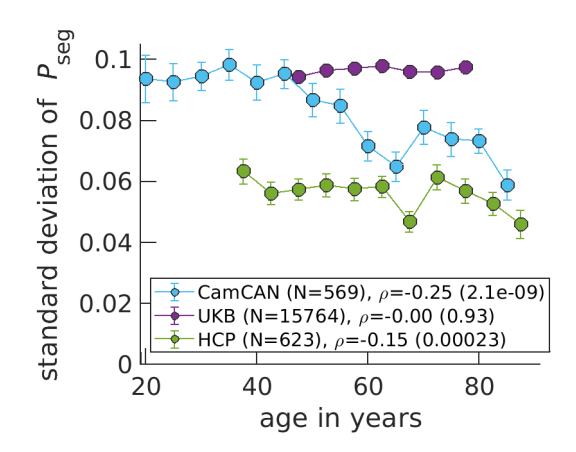


Figure S6. Standard deviations of P_{seg} per individual decreases as a function of age for CamCAN and HCP data sets. Data points correspond to medians, while error bars correspond to standard errors for bins of 5 years. The variable ρ corresponds to the Spearman correlation coefficient between age and P_{seg} calculated over all N individuals, with the p-value in parenthesis. Here, fMRI time-series data for an individual are equally split into 5 chunks and P_{seg} is calculated for each chunk before taking its standard deviation. In the main text, fMRI data are not split up and the entire time-series is considered in calculating

Authors: R.M. Razban, B.B. Antal, K.A. Dill, L.R. Mujica-Parodi

Table S2. Linear regression results for P_{seg} as a function of age

550

551

552

CamCAN	coefficient	t statistic	Prob $> t $	UK Biobank	coefficient	t statistic	Prob $> t $
intercept	0.575	40.0	8.66E-176	intercept	0.556	69.1	<1E-300
age	0.0028	11.1	3.03E-26	age	0.0013	9.92	4.06E-23

НСР	coefficient	t statistic	Prob $> t $
intercept	0.650	38.1	1.08E-171
age	0.0021	7.58	1.14E-13

 $\textbf{Table S3.} \quad \text{Multiple linear regression results for } P_{\text{seg}} \text{ as a function of age and sex across the data sets.}$

CamCAN	coefficient	t statistic	Prob $> t $	UK Biobank	coefficient	t statistic	Prob> $ t $
intercept	0.583	39.0	1.22E-170	intercept	0.561	70.8	<1E-300
sex(T.male)	-0.0163	-1.75	8.03E-02	sex(T.male)	-0.0445	-23.7	6.17E-122
age	0.0028	11.1	1.58E-26	age	0.0015	12.1	8.79E-34

НСР	coefficient	t statistic	Prob $> t $
intercept	0.668	39.6	1.92E-179
sex(T.male)	-0.0500	-6.17	1.20E-09
age	0.0022	8.03	4.21E-15

 Table S4.
 Multiple linear regression results for P_{seg} as a function of age, sex and handedness for the Human Connectome Project.

НСР	coefficient	t statistic	Prob> $ t $
intercept	0.677	32.8	5.75E-143
sex(T.male)	-0.0504	-6.20	9.72E-10
handedness(T.right)	-0.0095	-0.76	4.48E-01
age	0.0022	8.00	5.59E-15

Authors: R.M. Razban, B.B. Antal, K.A. Dill, L.R. Mujica-Parodi

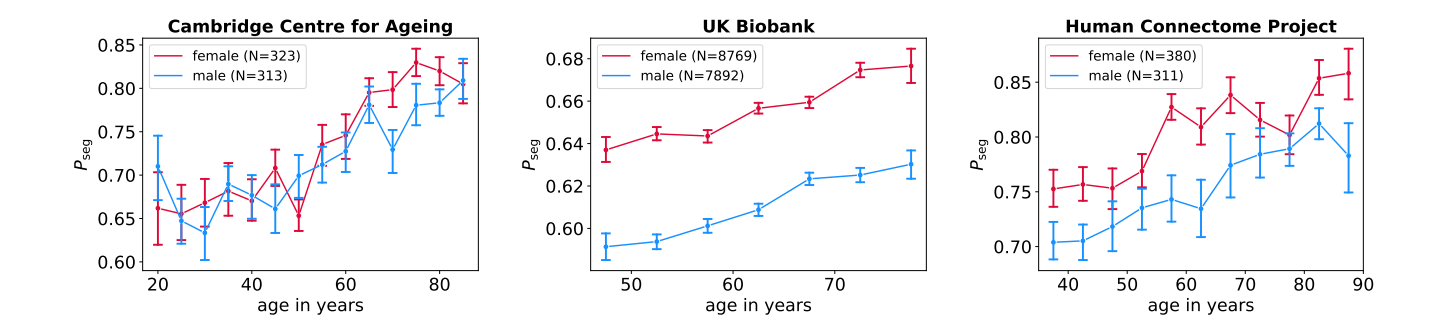


Figure S7. P_{seg} rises in aging brains across three data sets regardless of sex. Data points correspond to medians, while error bars correspond to standard errors for bins of 5 years. For UKB and HCP, we find that females' brains have higher shifted P_{seg} values across age.

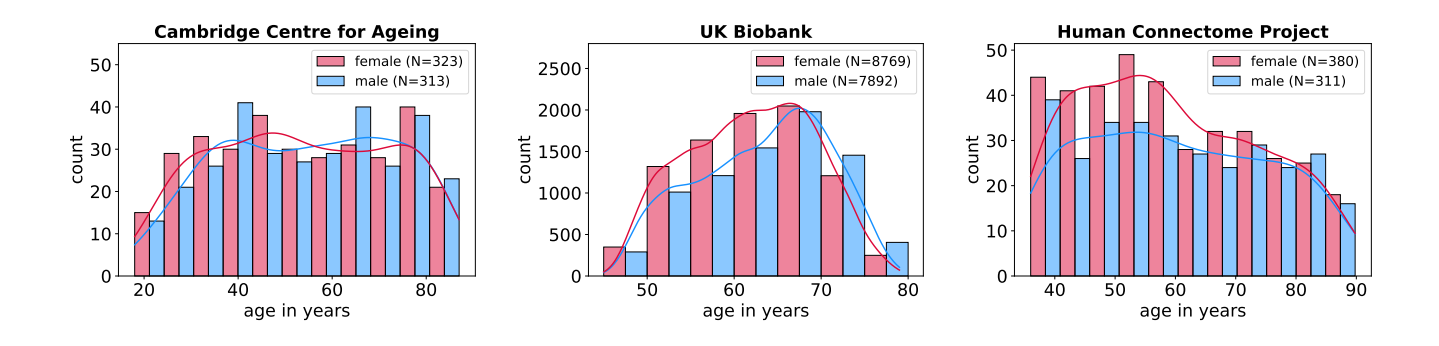


Figure S8. Sex is fairly well-represented across age across the three data sets. Thus, observed P_{seg} aging trends cannot be attributed to the increasing over-representation of one sex.

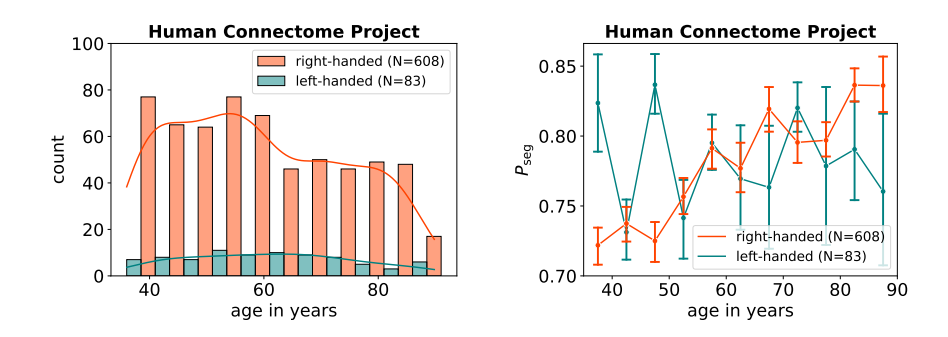


Figure S9. P_{seg} roughly rises in aging brains regardless of handedness. Data points correspond to medians, while error bars correspond to standard errors for bins of 5 years. Large error bars are seen for left-handed individuals because of small sample sizes (left plot).

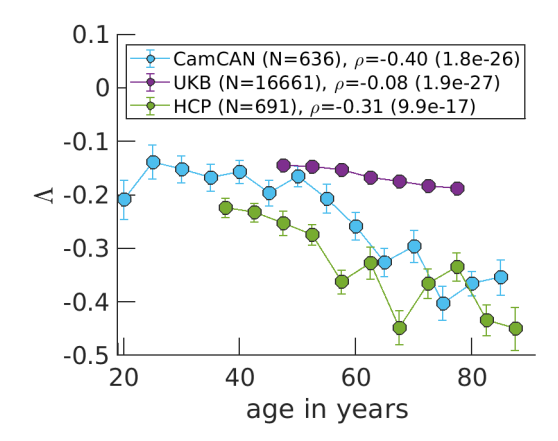


Figure S10. The rescaled connection strength parameter Λ moves further away from the critical point ($\Lambda=0$) as age increases. Trends are similar in form to Figure 3 because P_{seg} is a function of Λ (Equation 2). Data points correspond to medians, while error bars correspond to standard errors for bins of 5 years.

The variable ρ corresponds to the Spearman correlation coefficient between age and Λ calculated over all N individuals, with the p-value in parenthesis.

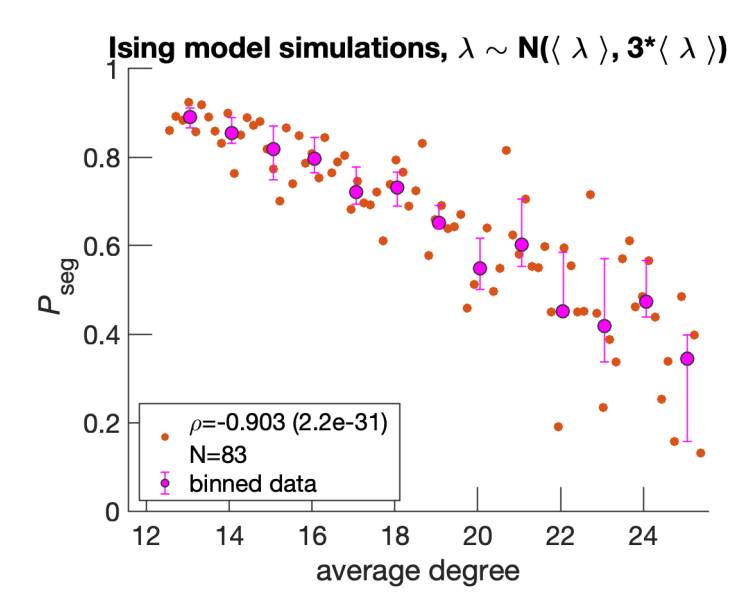


Figure S11. Greater variance in simulations is seen when edges' connection strengths λ are drawn from a normal distribution with mean $\langle \lambda \rangle$ and standard deviation $3 * \langle \lambda \rangle$. At each consecutive step, $\langle \lambda \rangle$ is attenuated such that 5 edges are effectively removed per step $(\langle \lambda' \rangle = \langle \lambda \rangle p_{\text{edge}})$ from the same starting dMRI structure as in Figure 4 (UK Biobank subject ID: 6025360). Data points correspond to medians, while error bars correspond to standard errors for bins of 5 years. Orange data points on the right plot correspond to individual Ising systems, where N reflects the total number. The variable ρ corresponds to the Spearman correlation coefficient calculated over all orange data points between average degree and P_{seg} , with the p-value in parenthesis. Magenta data points correspond to medians, while error bars correspond to upper and lower quartiles for bin sizes of one degree.

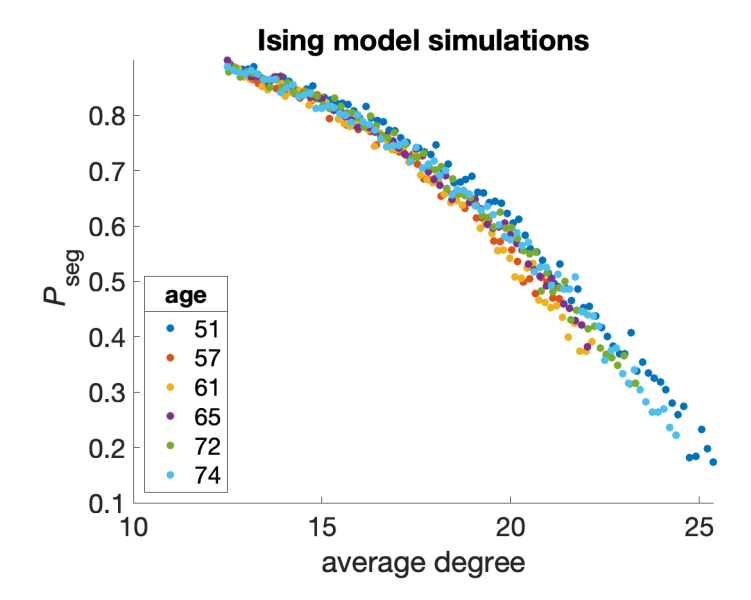


Figure S12. Similar results for Ising simulations are seen as in Figure 4 for different UK Biobank individuals with different ages. Edges are randomly removed as in Figure 4. Starting diffusion MRI structures are used from following subject IDs: 6025360 (51y), 4712851 (57y), 3081886 (61y), 1471888 (65y), 4380337 (72y), and 1003054 (74y).

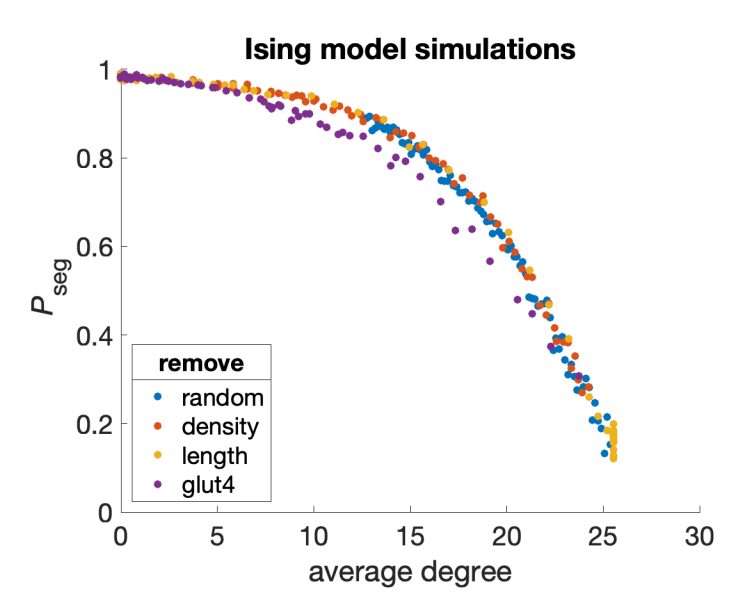


Figure S13. Edge removal mechanisms only matter in so much as they attenuate average degree for Ising simulations. In addition to randomly removing edges as shown in Figure 4, we computationally remove edges based on targeted attack of tract density, tract length, and a node's GLUT4 receptor density.

Edges are removed in sequential order, such that those with the largest value are removed first. For all properties except for random, we remove edges until none are present for the same starting dMRI structure as in Figure 4 (UK Biobank subject ID: 6025360).

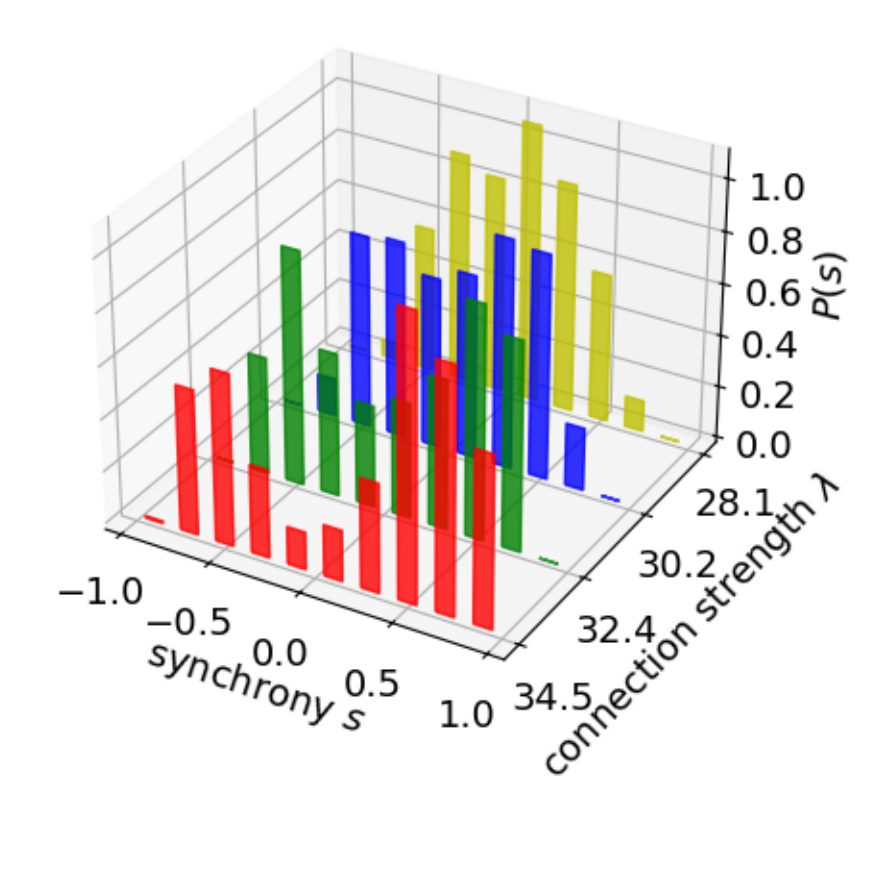


Figure S14. Synchrony distributions transform from bimodal to unimodal as edges are randomly removed from UK Biobank subject ID: 6025360. The parameter λ relates to edge removal because $\lambda = \lambda_0 * p_{\text{edge}}$, where λ_0 is a constant throughout the edge removal process and p_{edge} is the probability that two nodes share an edge (Methods).

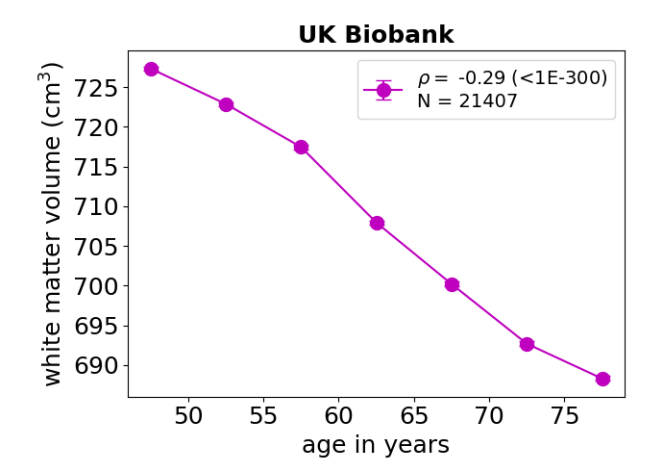


Figure S15. White matter volume decreases with age. White matter volume is measured by structural MRI provided by the UK Biobank. Data points correspond to medians, while error bars correspond to standard errors for bins of 5 years. The variable ρ corresponds to the Spearman correlation coefficient between age and white matter volume calculated over all N individuals, with the p-value in parenthesis. Error bars are plotted but are not visible because of their minuscule size. N is larger than that of Figure 3 because all individuals with structural MRI scans are considered.

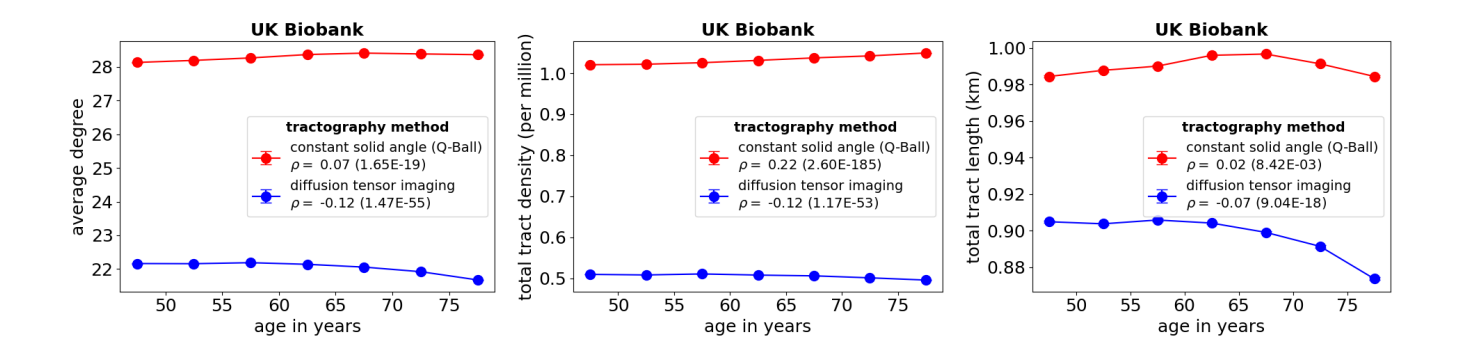


Figure S16. White matter tract properties do not degrade as a function of age when using the Q-Ball method for tractography. However, they do degrade with age when using the less accurate diffusion tensor imaging method. Data points correspond to medians, while error bars correspond to standard errors for bins of 5 years. The variable ρ corresponds to the Spearman correlation coefficient between age and the corresponding property calculated over all available individuals (N=16,649), with the p-value in parenthesis. Error bars are plotted but are not visible because of their minuscule size.

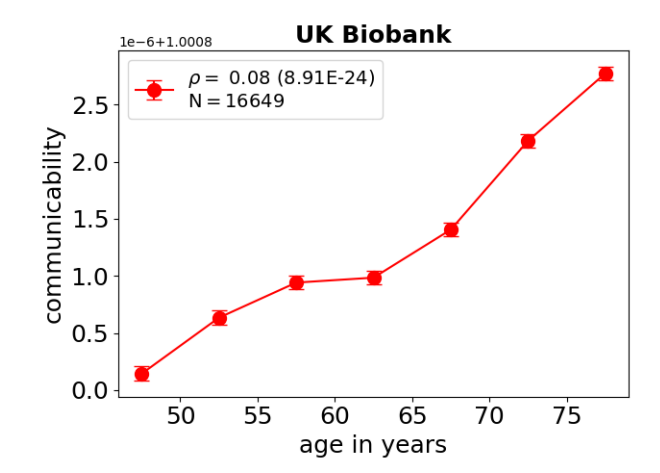


Figure S17. Mean communicability across all brain region pairs does not decrease with age. Communicability is calculated based on tract density as measured by the Q-Ball method for tractography (Methods). Data points correspond to medians, while error bars correspond to standard errors for bins of 5 years. The variable ρ corresponds to the Spearman correlation coefficient between age and white matter volume calculated over all N individuals, with the p-value in parenthesis. Note that the y-axis should be scaled by 10^{-6} and shifted by 1.0008.

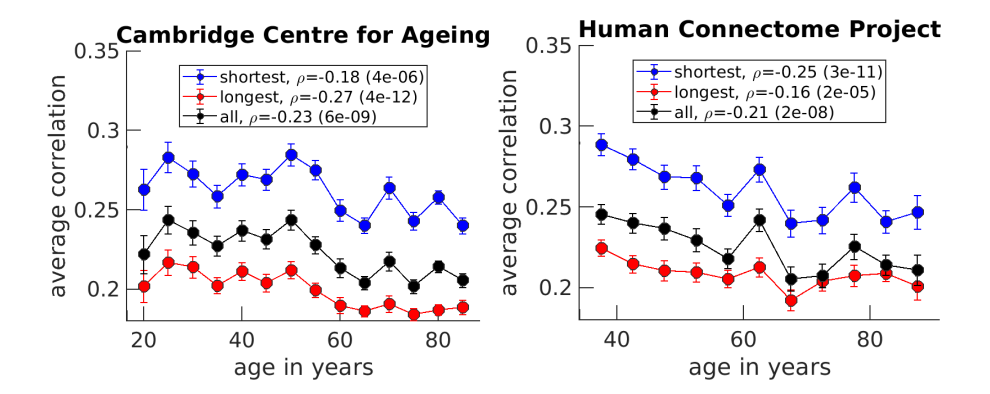


Figure S18. For the Cambridge Centre for Ageing and Neuroscience data set, the shortest edges (lower quartile) have average Pearson correlations or average functional connectivities which correlate less than those of the longest edges (upper quartile). For the Human Connectome Project, the opposite is the case. Edge distances are measured by center of mass coordinates of the brain regions based on the Seitzman atlas. Shortest and longest edges correspond to the lower and upper quartile (25%), respectively. Only positive correlations are considered and diagonal elements are ignored. Data points correspond to medians, while error bars correspond to standard errors for bins of 5 years. The variable ρ corresponds to the Spearman correlation coefficient between age and average correlation calculated over all available individuals ($N_{CamCAN} = 640$ and $N_{HCP} = 700$), with the p-value in parenthesis.

Authors: R.M. Razban, B.B. Antal, K.A. Dill, L.R. Mujica-Parodi

596 **Table S5.** Functional MRI acquisition parameters of the data sets.

597

Data set	field strength	repetition time	echo time	flip angle	voxel size	total time points
CamCAN	3T	1970 ms	30 ms	78°	$3x3x4.44 \text{ mm}^3$	241
UK Biobank	3T	735 ms	39 ms	52°	2.4x2.4x2.4 mm ³	490
НСР	3T	800 ms	37 ms	52°	$2x2x2 \text{ mm}^3$	1912

Table S6. Demographic information of the data sets for those individuals in Figure 3.

Data set	age range	$\langle age \rangle \pm std(age)$	sex
CamCAN	18-87	54.2±18.6	323F/313M
UK Biobank	45-79	54.8±7.4	8769F/7892M
НСР	36-90	59.6±14.9	380F/311M

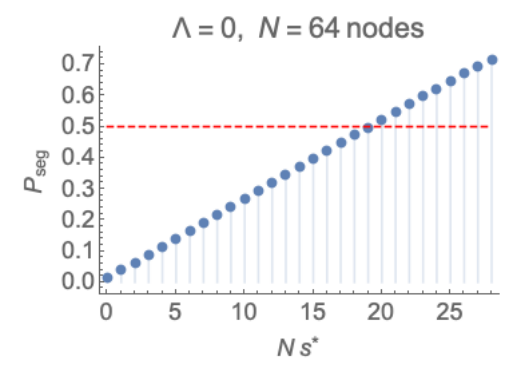


Figure S19. The synchrony threshold s^* is chosen such that it delineates between integrated and segregated states when $P_{\text{seg}} = P_{\text{int}} = 1/2$ (red line) at the critical point ($\Lambda = 0$). This particular figure is created for 64 nodes; it must be set to the corresponding data set's N_{eff} to determine the appropriate synchrony threshold.

Authors: R.M. Razban, B.B. Antal, K.A. Dill, L.R. Mujica-Parodi

TECHNICAL TERMS

- Integration a network state composed of global signaling.
- Segregation a network state limited to local signaling.
- State a particular combination of physical properties. Here, we assume that brain networks can only occupy either the integrated or segregated state.
- Ising model a classic model in physics that was first applied to ferromagnetism. It includes pairwise interactions between binary spin states.
- Phase interchangeable with the word 'state' for the purposes of this text.
- Critical Point the point where two phases coexist. In this text, it is where the synchrony distribution dramatically changes from bimodal (primarily integrated) to unimodal (primarily segregated).
- Maximum Entropy fit a fitting strategy that satisfies user-defined constraints in the most agnostic way.
- White Matter bundles of axons connecting brain regions.